A High-Efficiency Flyback Micro-inverter With a New Adaptive Snubber for Photovoltaic Applications

Mohammad Ali Rezaei, Kui-Jun Lee, and Alex Q. Huang, *Fellow, IEEE*

***Abstract*—Based on the hybrid operation of interleaved flyback micro-inverter in discontinuous and boundary conduction modes (DCM and BCM), a novel adaptive snubber is proposed in this paper. The proposed snubber limits the drain-to-source voltage overshoot of the flyback's main switch during the turn-off process, enabling the use of lower voltage MOSFETs. It also recovers the stored energy in the leakage inductance of the flyback transformer and provides soft switching for the main flyback switch by limiting the rising slope of the MOSFET voltage during the turn-off process resulting in higher efficiency. Exploiting the natural resonant of the flyback converter in BCM, the adopted controller provides ZVS and ZCS for the main switch during the BCM operation. The operation of the flyback micro-inverter with associated controllers is analytically studied, and considerations for an optimum design aiming to higher efficiency are presented. Performance of the flyback micro-inverter with the proposed adaptive snubber and the corresponding controllers is experimentally verified based on a 250W interleaved flyback micro-inverter hardware setup.**

***Index Terms*—Flyback, high efficiency, micro-inverter, snubber.**

I. Introduction

PHOTOVOLTAIC (PV) micro-inverters have gained a significant attention for grid-connected PV system applications during the past few years because of improved energy harvest, friendly "Plug-N-Play" operation, and enhanced modularity and flexibility [1]–[3]. Various inverter topologies for PV micro-inverters applications have been introduced in the literature that perform the maximum power point tracking (MPPT) of PV module, high step-up voltage amplification, output current shaping, and galvanic isolation [1], [3]. Among them, the flyback-based micro-inverter is one of the most attractive solutions due to its simple structure and control and also inherent galvanic isolation.

Fig. 1 illustrates the conventional flyback micro-inverter, which consists of decoupling capacitor(s), interleaved flyback converter, unfolding bridge, and *CL* filter. The unfolding bridge is switched at line frequency by a simple square-wave control, generating a rectified sinusoidal waveform at the dc link between the interleaved flyback converter and unfolding bridge. The decoupling capacitor, which consists of several parallel connected electrolytic capacitors, maintains the power balance between the constant input power and variable output power oscillating at double-line frequency. All the other functionalities required in PV micro-inverter are performed by the flyback converter. Therefore, the flyback converter has been widely scrutinized to improve its performance in terms of efficiency, reliability, and cost.

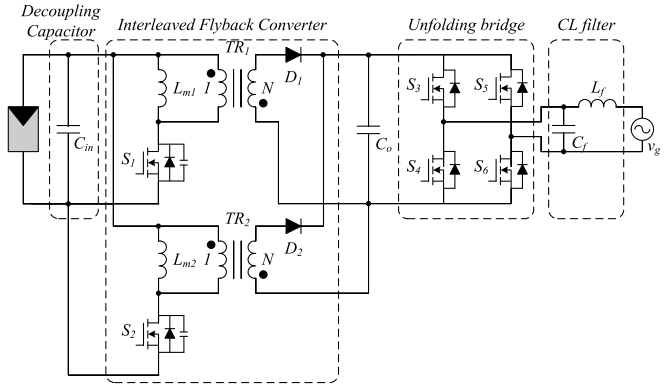

Fig. 1. Flyback micro-inverter for the PV application.

In order to improve efficiency and power density, the DCM and BCM operations of the flyback micro-inverter have been comprehensively analyzed and a hybrid switching strategy has been adopted [4], [5]. To further improve the weighted efficiency of the micro-inverter system, synchronous rectification at the high-voltage side of the flyback inverter is employed in [6], which leads to slight improvement in the overall efficiency.

A non-complementary active clamp control method is proposed to achieve high efficiency both for full-load and light-load conditions by reducing a circulating energy [7]. Furthermore, appropriate design parameters under the DCM operation have been specified to obtain maximum weighted efficiency through analytical loss calculation [8], and adaptive active clamping and phase control method [9] and hybrid control strategy combining two-phase and one-phase DCM control [10] have been proposed to improve weighted efficiency according to the output power of a PV module. Using a center-tapped transformer and bidirectional switches on the grid side, a turn-on ZVS approach is proposed in [11], which utilizes snubber to maintain the voltage spike within limits.

In [12], an open-loop controller based on the primary current feedback in the continuous conduction mode (CCM) operation has been proposed to accommodate a right-half-plane zero in the control to output current transfer function; thus, it showed an efficiency improvement compared to the DCM scheme. A

Manuscript received July 20, 2014; revised October 26, 2014; accepted November 20, 2014. Date of publication March 5, 2015; date of current version September 21, 2015. This work was supported in part by the U.S. Department of Energy under Award DE-EE-0006036 and made use of ERC shared facilities supported by the National Science Foundation under Award EEC-0812121. Recommended for publication by Associate Editor T. Suntio.

M. A. Rezaei and A. Q. Huang are with the Future Renewable Electric Energy Delivery and Management Systems Center of North Carolina State University, Raleigh, NC 27606 USA (e-mail: mrezaei@ncsu.edu; aqhuang@ncsu.edu).

K.-J. Lee is with Samsung Electronics, Suwon 442-742, Korea (e-mail: klee14@ncsu.edu).

Color versions of one or more of the figures in this paper are available online at http://ieeexplore.ieee.org.

Digital Object Identifier 10.1109/TPEL.2015.2407405

through dynamic modeling and control of an interleaved flyback micro-inverter along with a two-step controller design based on realistic fourth-order system modeling including the dynamics of the output *CL* filter is presented in [13], which aims to compensate the instability issue of the converter working in CCM. Also, in order to reduce the cost and complexity of the flyback micro-inverter system, the idea of multiple-integrated converter modules sharing a single unfolding bridge is presented in [14] based on the flyback micro-inverter operating in CCM.

A procedure for selecting the decoupling capacitors in the flyback micro-inverter working in DCM considering the PV power utilization and the total harmonic distortion (THD) of the output current in presented in [15]. Although the electrolytic capacitors are suitable candidate as power decoupling storage elements due to their large capacitance and low cost, they are the major limiting factor of the inverter lifetime. Therefore, a three-port flyback converter, with one port is dedicated to power decoupling [16], and its advanced version with reduced components [17] have been proposed to enable a small film capacitor to be used instead of the bulky and unreliable electrolytic capacitor.

The phase synchronization control strategies of an interleaved flyback inverter operating in BCM are analyzed in [18], and in order to reduce the switching loss associated with the current mismatch in two phases on the inverter, a closed-loop phase synchronization control method is proposed.

Following these efforts, this paper presents a novel adaptive snubber to enhance the performance of the flyback micro-inverter operating in the hybrid mode. The proposed adaptive snubber combines the simplicity of RCD snubber and efficiency of active clamp circuits to achieve a high efficiency at lowest possible cost.

The proposed snubber consists of an auxiliary switch and a snubber capacitor, which is similar to the conventional active clamping circuit, but with different control scheme and design procedure. The lower snubber capacitance and simple gate driving signal for the auxiliary switch makes it possible to achieve high efficiency at low implementation cost.

Effectiveness of the proposed snubber is experimentally validated through experimentation on a 250-W flyback micro-inverter prototype.

II. Conventional Flyback Micro-inverter With Active Clamping

Fig. 2(a) illustrates the conventional flyback micro-inverter with the active clamping circuit to improve the weighted efficiency [9]. It should be noted that output unfolding stage is replaced with the equivalent rectified sinusoidal voltage source in order to simplify the analysis of the operational modes.

This flyback converter is normally operated in CCM or DCM and uses the active clamping circuit to clamp the voltage across the main switch, and prevent voltage overshoot at turn-off and achieve ZVS turn-on of the main switch. This enables the operation of the converter with higher efficiency through soft switching and also the use of MOSFET with lower $R_{ds(\mathrm{on})}$. Furthermore, the non-complementary gate driving signal for

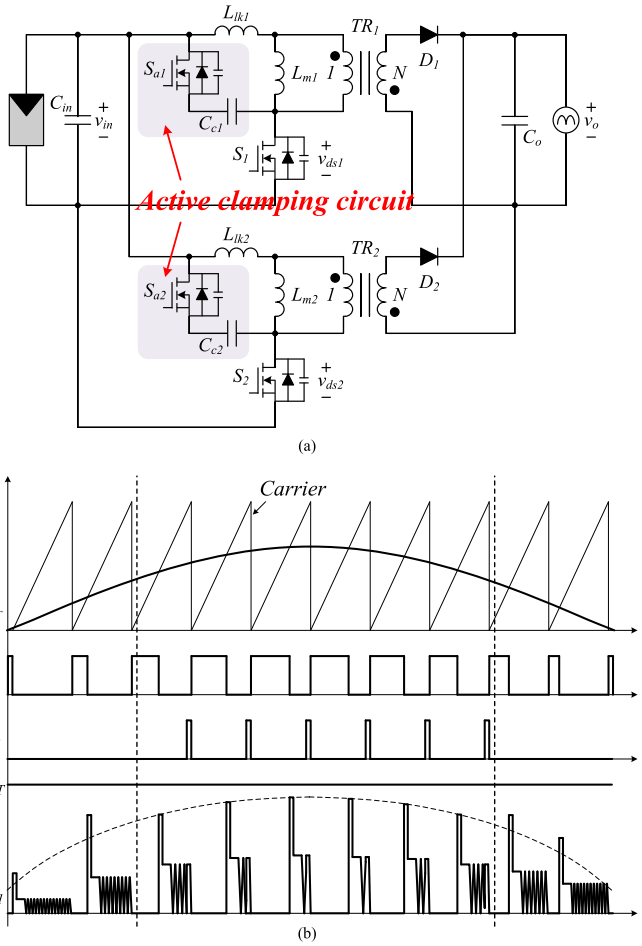

Fig. 2. Conventional active clamping circuit in flyback micro-inverter. (a) Circuit configuration. (b) Main operation waveforms.

the active clamp switch presented in [9] can reduce the circulating energy compared to the conventional complementary control signal [7], and the hybrid control method that disables the active clamp circuit at the low grid voltage improves the weighted efficiency by reducing the switching, conduction, and gate driving loss of the active clamp switch. However, as it is shown in Fig. 2(b), the noncomplementary gate signal still uses a high-frequency switching, which increases the driving loss. Also, the active clamping circuit requires relatively a large capacitance in a range of hundreds of nanofarads, which is costly and bulky. Although a PMOS-based active clamp circuit can be used to simplify the clamp switch gate drive, its performance and cost are not comparable with NMOS; thus, the additional isolated power supply required for driving the active clamp switch adds to the cost and complexity of the micro-inverter system.

III. Proposed Flyback Micro-inverter With Adaptive Snubber

Fig. 3(a) shows the proposed flyback micro-inverter with the novel adaptive snubber, which is suitable for use in converter operating with hybrid conduction mode as it is shown in Fig. 3(b). The configuration of the adaptive snubber is similar to the

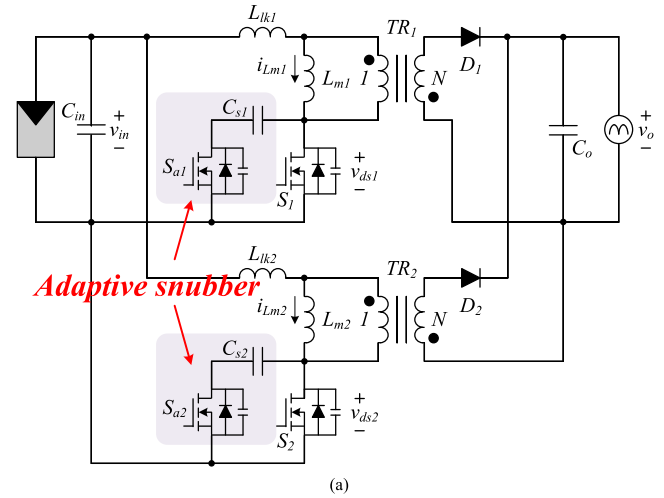

Fig. 3. Proposed adaptive snubber scheme in flyback micro-inverter. (a) Circuit configuration. (b) Main operation waveforms.

previous active clamping circuit. However, the control scheme and the design procedure of the proposed adaptive snubber are entirely different.

The BCM operation of the flyback converter has several advantages compared to the DCM operation in terms of power density and conversion efficiency. Since the BCM operation provides a natural ZVS turn-on for the main switch, the reduced switching loss allows higher switching frequency and compact design. However, it still has the turn-off switching loss that limits the maximum allowable switching frequency. Also, during the BCM operation of the converter and near the peak grid voltage where the instantaneous transferred power is high, the leakage inductance in flyback converter causes voltage overshoot across the main switch at turn-off and the turn-off switching loss becomes more severe.

The proposed snubber solves these problems by adding a capacitor in parallel with the main switch. This capacitor reduces the voltage overshoot and also lowers the rising slope of the turn-off voltage. These effects allow low conduction loss from the

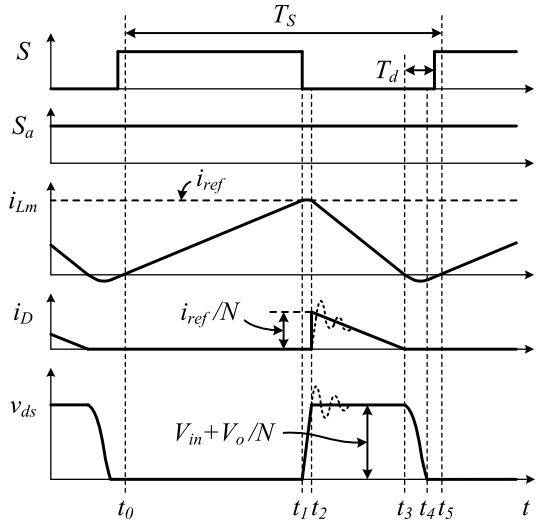

Fig. 4. Theoretical operation waveforms under BCM.

usage of lower voltage rating device and also reduce the turn-off switching loss of the main switch. This additional capacitor does not affect the soft switching of the main switch at turn-on if enough time delay is applied between zero crossing of magnetizing current and the next turn-on switching signal.

Since natural turn-on ZVS is not guaranteed during the DCM operation, the turn-on switching loss associated with the additional capacitor becomes dominant and the reduction of turn-off switching loss becomes marginal. Therefore, to improve the overall efficiency of the flyback micro-inverter, as shown in Fig. 3(b), an auxiliary switch is employed to disconnect the snubber capacitor from the circuit when the converter works in the DCM mode. As a result, during the DCM operation of the converter, the auxiliary switch (S_a) is OFF and during the BCM operation, when the natural turn-on ZVS is achievable, the auxiliary switch is always ON, effectively adding the capacitor C_s across the drain-source terminals of the main switch.

The proposed adaptive snubber provides the same advantages as the conventional active clamping method in terms of zero-voltage switching and also limiting the voltage across the main switch at turn-off at a much lower cost. Furthermore, the auxiliary switch is operated at only double-line frequency and the required snubber capacitance is very small, in range of tens of nanofarad, which is more than ten times smaller than the required capacitance value in the conventional active clamping. Also, the additional isolated power supply for driving the auxiliary switch is not required any more since an N-channel MOSFET can be used that shares the same source terminal with the main MOSFET. All these advantages reduce the cost and complexity and also increase the overall efficiency of the PV micro-inverter system.

A. *Operation Principle*

Fig. 4 shows the theoretical operation waveforms of the proposed flyback micro-inverter under BCM during one switching period T_S, and Fig. 5 shows the equivalent circuits for each operation mode.

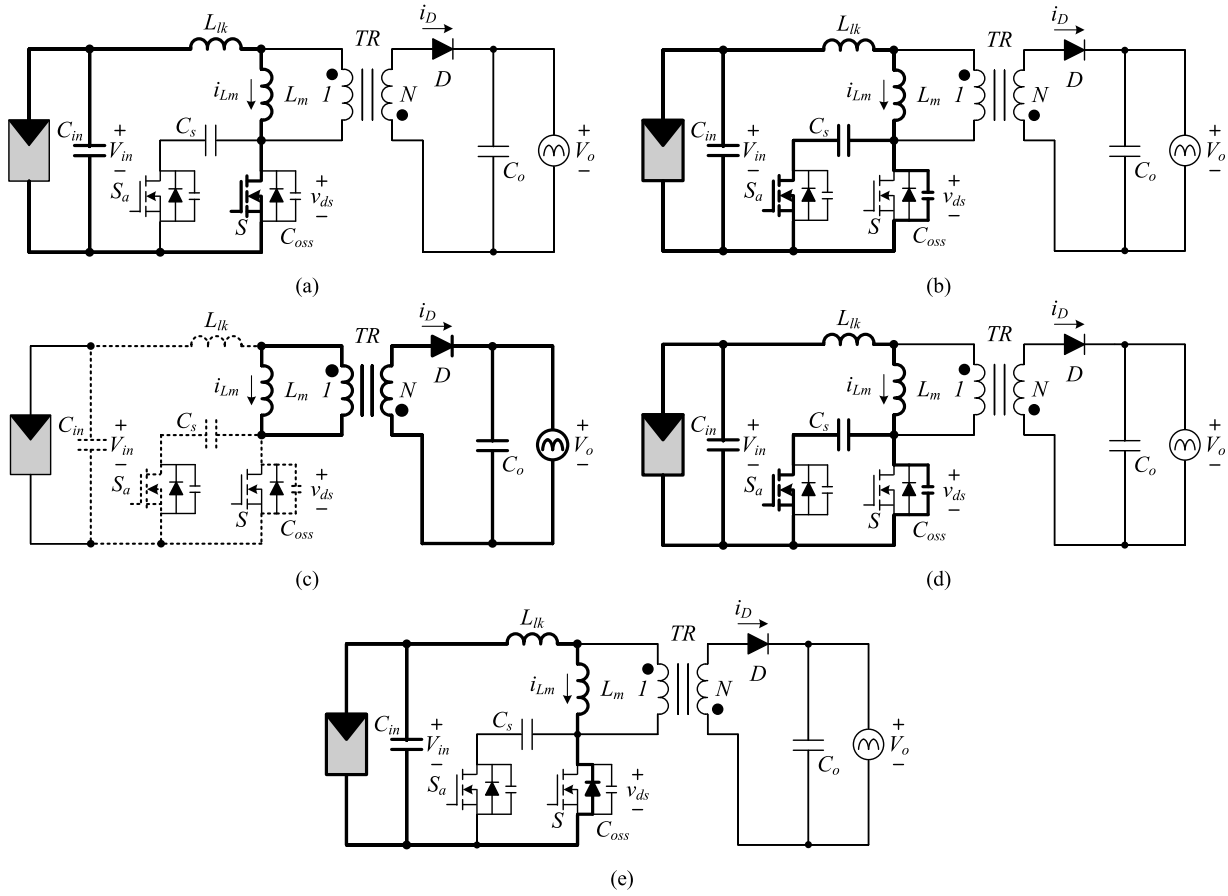

Fig. 5. Equivalent circuits for each operational mode: (a) Mode 1 [t_0–t_1]. (b) Mode 2 [t_1–t_2]. (c) Mode 3 [t_2–t_3]. (d) Mode 4 [t_3–t_4]. (e) Mode 5 [t_4–t_5].

To simplify the circuit analysis, only one flyback converter is considered due to the fact that converters operate in the same manner in interleaved mode. Also, the voltages $V_{\rm in}$ and V_o and the reference current $i_{\rm ref}$ are assumed to be constant during T_S. Furthermore, the auxiliary switch S_a is always in the ON state, since the converter operates under BCM. Each operation mode is described next.

1) Mode 1 (t_0–t_1): Just before t_0, the switch S has turned ON. The magnetizing inductor current i_{Lm} increases linearly from zero until it reaches $i_{\rm ref}$. At this moment, the switch S turns OFF and *Mode 1* ends. The required time in this mode is

$$\begin{aligned} t_{01} &= \frac{L_{\rm tot}}{V_{\rm in}}.\, i_{\rm ref} \\ L_{\rm tot} &= L_m + L_{lk} \approx L_m. \end{aligned} \tag{1}$$

Although the $i_{\rm ref}$ is assumed to be constant during T_S, the actual value of the $i_{\rm ref}$is continuously changing across the grid period [10], [19], as

$$i_{\rm ref} = \begin{cases} \sqrt{\dfrac{2T_{\rm DCM}P_o}{L_m}} \cdot \sin\omega t, & \text{in DCM} \\ \left(\dfrac{\sqrt{2}V_o \sin\omega t}{V_{\rm in}} + N\right) \cdot \sqrt{2}\dfrac{P_o}{V_o} \sin\omega t, & \text{in BCM} \end{cases} \tag{2}$$

where $T_{\rm DCM}$ is the switching period in DCM, P_o is the output power of the interleaved converter, ω is the angular frequency of the grid voltage, and *N* is the transformer turns ratio.

2) Mode 2 (t_1–t_2): At t_1, switch S turns OFF and the resonance between inductors (L_m, L_{lk}) and capacitors (C_s, C_{oss}) begins where C_{oss} is the parasitic capacitance of the switch S. The resonant frequency is given by

$$\begin{aligned} f_{\rm res} &= \frac{1}{2\pi\sqrt{L_{\rm tot}C_{\rm tot}}} \\ C_{\rm tot} &= C_s + C_{oss} \approx C_s. \end{aligned} \tag{3}$$

The duration of this mode is relatively short as compared to the whole resonant period due to the large value of the magnetizing inductor current at turn-off; thus, the voltage v_{ds} increases almost linearly. This mode ends when the voltage v_{ds} reaches $V_{\rm in} + V_o/N$. Duration of this, mode can be approximated by

$$t_{12} = \frac{C_{\rm tot}}{i_{\rm ref}} \cdot \left(V_{\rm in} + \frac{V_o}{N}\right). \tag{4}$$

As it is shown in (4), addition of the snubber capacitor C_s causes t_{12} to increase, which effectively reduces the rising slope of the voltage v_{ds1} and allows the turn-off process to be soft and almost lossless.

3) Mode 3 (t_2–t_3): The energy stored in the magnetizing inductor L_m is transferred to the output side. The output diode current i_D linearly decreases to zero, thus the reverse-recovery

effect of *D* is minimized. If the leakage inductance is assumed to be zero as ideal condition to simplify the operational analysis, the voltage v_{ds} maintains the constant value of $V_{\rm in} + V_o/N$ during this mode. However, in the real case, the leakage inductance causes a high-frequency oscillation at the beginning of this mode, as it is shown in the dotted waveforms of Fig. 4. The conduction path of the oscillating current is also shown in Fig. 5(c) with dotted lines. Without a snubber or clamping circuit to protect the main switch, this voltage spike enforces the use of a high-voltage rated switching device. The duration of this mode can be calculated as

$$t_{23} = \frac{L_m}{V_o/N} \cdot i_{\rm ref}. \tag{5}$$

4) Mode 4 (t_3–t_4): This is a resonant mode similar to Mode 2. If the steady-state value v_{ds} at during Mode 3 satisfies the following equation:

$$V_{\rm in} + V_o/N > 2V_{\rm in} \;\rightarrow\; V_o > NV_{\rm in} \tag{6}$$

the voltage v_{ds} decreases to zero with a resonant manner within the maximum of half resonant period as shown in (7) regardless of the amount energy stored in the magnetizing inductance

$$t_{34} \le \pi\sqrt{L_{\rm tot}C_{\rm tot}}. \tag{7}$$

5) Mode 5 (t_4–t_5): While the current i_{Lm} flows negatively through the antiparallel diode of the switch S, the gating signal of the switch S is applied, thus satisfying the ZVS turn-on. The time delay T_d between the zero magnetizing current and the turn-on of switch S is given by the half the resonant period, which is the maximum value of (7).

B. Improved Reference Current

In the flyback micro-inverter, the reference current is very important because it directly affects the output current THD. The reference current in (2) is obtained by assuming the ideal conditions without considering the resonant modes in Modes 2 and 4. However, in the proposed flyback micro-inverter, these resonant modes cannot be ignored during the BCM operation due to the added snubber capacitor. In particular, since the resonant period t_{34} of (7) is dominant compared to the t_{12} of (4), the reference current is modified only considering t_{34} in this paper.

Fig. 6 shows the average output current during BCM operation with quasi-resonant mode. The average output current proportional to the shaded triangle area. Therefore, it can be obtained as

$$i_{g\_\rm avg} = \frac{t_{\rm off}\, i_{\rm ref}}{2TN}, \quad T = t_{\rm on} + t_{\rm off} + t_{QR}. \tag{8}$$

From (8), the improved reference current can be obtained as

$$\begin{aligned} i_{\rm ref} &= \frac{2TN}{t_{\rm off}} i_{g\_\rm avg} \\ &= \frac{A + \sqrt{A^2 + 4B}}{2} \\ A &= 2\left(\frac{\sqrt{2}V_g \sin\omega t}{V_{\rm in}} + N\right)\left(\sqrt{2}\frac{P_o}{V_o}\sin\omega t\right) \end{aligned}$$

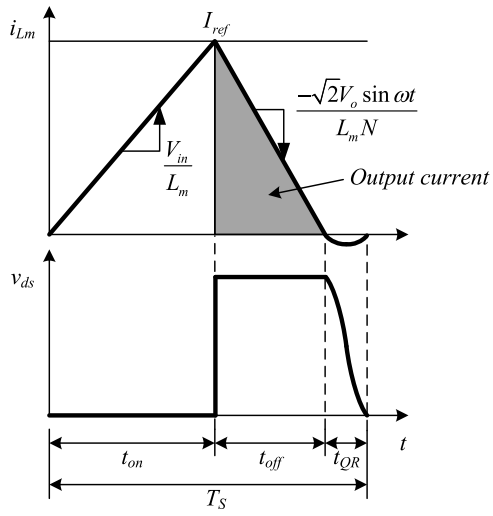

Fig. 6. Average output current during BCM operation.

$$B = 2\pi\sqrt{\frac{C_{\rm tot}}{L_m}}\sqrt{2}V_g \sin\omega t \cdot \left(\sqrt{2}\frac{P_o}{V_o}\sin\omega t\right). \tag{9}$$

Fig. 7(a) shows the original reference current of (2) in each operational mode and the improved one of (9) in the BCM operation. Furthermore, Fig. 7(b) shows the amplitude ratio of the improved to the original reference in BCM. It can be noticed that the ratio is almost constant for the middle range of grid period corresponding to the actual BCM operation. Therefore, for simple implementation, a constant value of around 1.1 can be multiplied to the original reference in BCM instead of directly using the complex equation of (9).

C. Design Considerations

1) Magnetizing Inductance L_m: The value of magnetizing inductance L_m is an important parameter in the BCM due to its direct relationship to the switching frequency. In PV micro-inverter application, the switching frequency becomes lowest near the peak grid voltage. Therefore, the lowest switching frequency can be determined in that point. From the previous mode analysis, the switching frequency can be approximately obtained as

$$f_s = \frac{1}{T_s} \approx \frac{1}{t_{01} + t_{12} + t_{23} + T_d}. \tag{10}$$

Fig. 8 shows the lowest switching frequency according to the snubber capacitance by using (10), where the leakage inductance is assumed to be 1% of the magnetizing inductance. Compared to the ideal case of $C_{\rm tot} = 0$ nF, the actual switching frequency decreases due to the additional resonant period of Mode 2 and Mode 4. In this paper, the magnetizing inductance is selected as 6 μH considering some margins based on the lowest switching frequency of 100 kHz since the actual power conversion loss requires a little higher reference current compared to the ideal case.

2) Snubber Capacitor C_s: The value of snubber capacitor C_s is selected to minimize the spike voltage across the main switch during Mode 3. Although a relatively large snubber

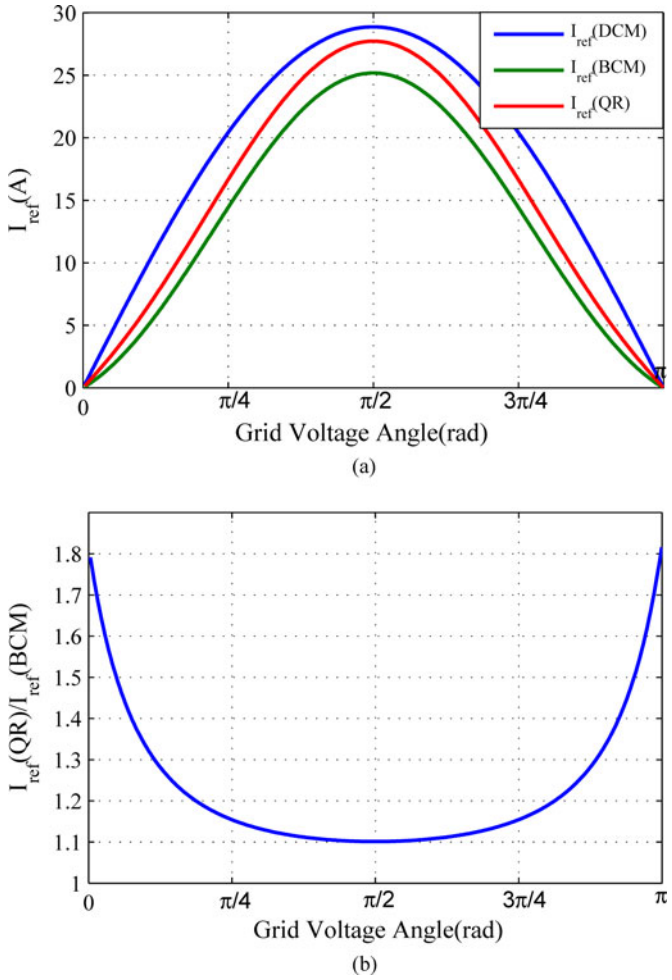

Fig. 7. Reference current considering $F_{\mathrm{DCM}} = 100\,\mathrm{kHz}$, $N = 6$, $P_o = 250$ W, $V_o = 240$ V, $L_{\mathrm{tot}} = 6\,\mu\mathrm{H}$, and $C_{\mathrm{tot}} = 10\mathrm{nF}$. (a) Comparison between DCM, ideal BCM, and BCM considering t_{QR} in Mode 4. (b) Amplitude ratio of improved to original reference in BCM.

capacitor can effectively reduce the spike voltage, it increases the duration of oscillations during the turn-off process, which results in low overall efficiency. Large snubber capacitor also increases the resonant time of Mode 4 (t_{QR}), which can result in lower switching frequency and higher output current THD. Furthermore, it leads to high cost and volume so, it should be appropriately restricted to the lowest possible value. The peak voltage across the main switch S is calculated as [9]

$$v_{ds\_\mathrm{peak}} = v_{\mathrm{in}} + \frac{v_o}{N} + v_{\mathrm{spike}}$$
$$v_{\mathrm{spike}} = i_{Lm\_\mathrm{peak}}\sqrt{\frac{L_{lk}}{C_{\mathrm{tot}}}} \tag{11}$$

where v_{spike} is the spike voltage caused by the resonance of L_{lk} and C_{tot}, and i_{Lm_peak} is the peak magnetizing inductance current.

Fig. 9 shows the peak voltage across the main switch according to the leakage inductance by using (11) with $P_o(=250\,\mathrm{W})$, $v_{\mathrm{in}}(=30.6\,\mathrm{V})$, $v_o(=240\,\mathrm{Vrms})$, $N(=6)$, and $L_m(=6\,\mu\mathrm{H})$. Fig. 9(a) shows the relationship between v_{ds_peak} and C_{tot} with the fixed grid angle ($=\pi/2$ rad), and Fig. 9(b) shows the

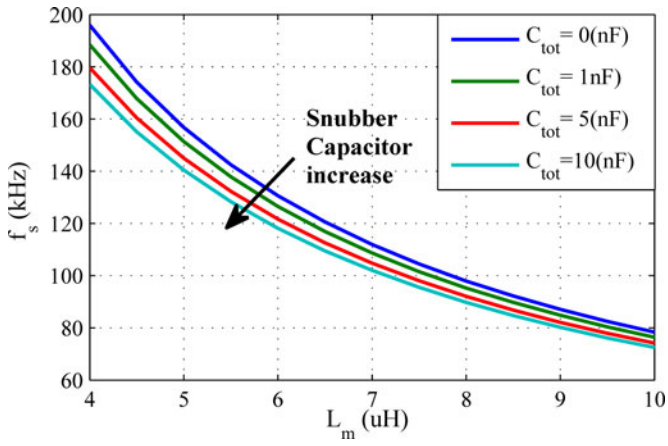

Fig. 8. Minimum value of switching frequency in BCM versus magnetizing inductance for maximum power of 250 W in a 240-V system.

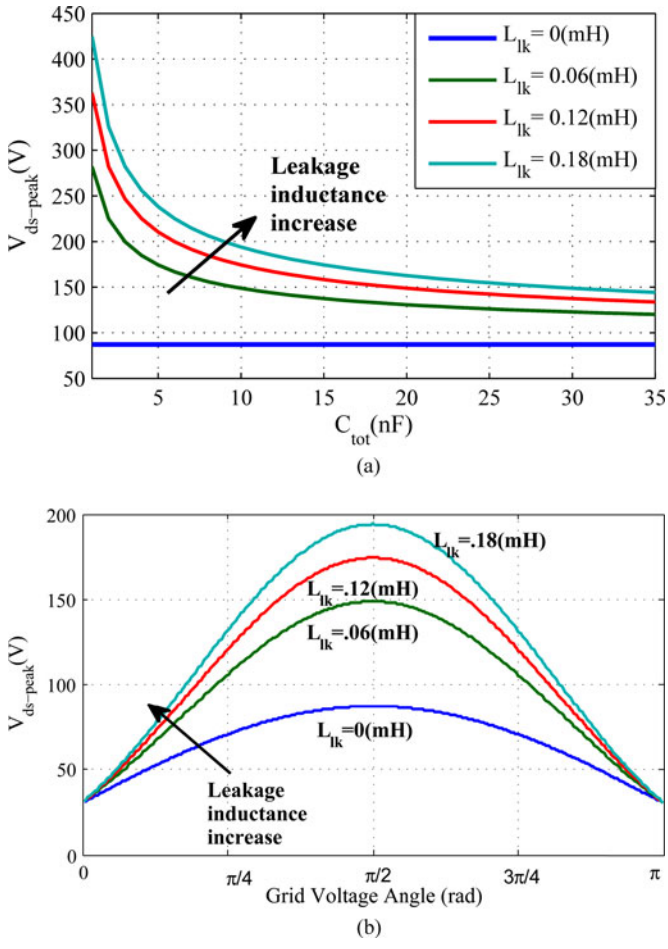

Fig. 9. Peak voltage across the main switch according to the leakage inductance. (a) Grid angle $= \pi/2$ (rad). (b) $C_{\mathrm{tot}} = 10$ (nF).

relationship between v_{ds_peak} and grid angle with the fixed $C_{\mathrm{tot}}(=10\,\mathrm{nF})$. The solid blue line in Fig. 9 shows the ideal case corresponding to the zero leakage inductance. However, as shown in Fig. 9(a), the peak voltage is not only proportional to the leakage inductance but also extremely increased with only a few percent leakage inductances in case of small snubber

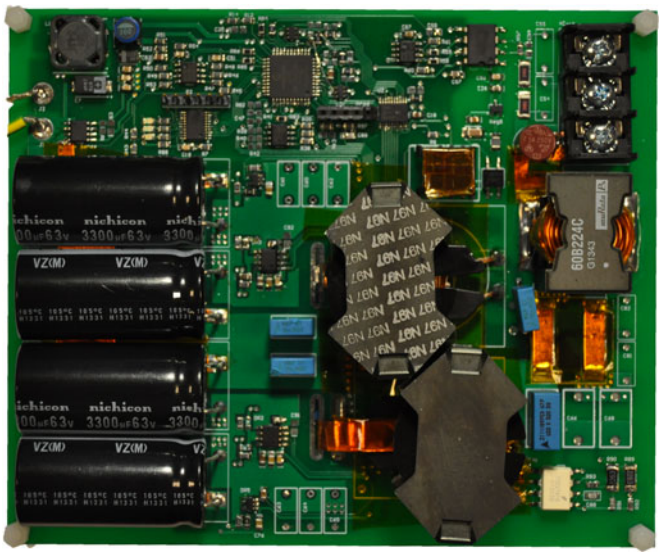

Fig. 10. Photograph of the experimental prototype.

capacitance. Therefore, based on the leakage inductance of the designed transformer, the relevant snubber capacitance can be selected by Fig. 9(a). For example, if the leakage inductance is assumed to be 0.06 μH corresponding to the 1% magnetizing inductance, it requires at least 10 nF of $C_{\rm tot}$ to maintain $v_{ds\_{\rm peak}}$ below 150 V.

In order to select the proper value for the snubber capacitor, it is important to calculate the required $C_{\rm tot}$ based on (11). However, it should be considered that since the required capacitance is usually in order of nanofarads, the stray capacitances of a real hardware can be exploited to further reduce the value of the snubber capacitor. Specifically, as it is mentioned in [9] and [20], the capacitance of the primary winding of transformer and also the reflected anode–cathode capacitance of the secondary rectifier are effectively in parallel with C_{oss} during the switching transients, so, the most suitable equation for calculating the required snubber capacitance can be deduced as

$$v_{\rm spike} = i_{Lm\_{\rm peak}} \sqrt{\frac{L_{Lk}}{C_{oss} \,\|C_s\, \|C_{\rm pw}\, \|N^2 C_D}} \qquad (12)$$

where $C_{\rm pw}$ is the primary winding capacitance of the flyback transformer and C_D is the anode–cathode capacitance of the secondary rectifier.

Another important property of a real hardware that can be exploited to reduce the required snubber capacitance is the nonlinearity of a MOSFET's C_{oss}. The value of C_{oss} at low voltages can be more than 10× higher than its value in higher voltages, which further helps to damp the voltage overshoot and reduce the value of required snubber capacitor.

3) Auxiliary switch S_a: The current rating of the auxiliary switch S_a is small since it only carries current during Modes 2, 3 and 4. Furthermore, the switching frequency is quite low so that the switching loss can be ignored. Therefore, a very slow MOSFET with low $R_{ds(\rm on)}$ can be used. The operation of the auxiliary switch is determined by the operational mode.

TABLE I
SYSTEM SPECIFICATIONS

Output Power (P_o)		250 W
Input Voltage (v_{in})		24 ~ 35 V
Grid Voltage (v_g)		240 Vrms
Grid Frequency (f_g)		60 Hz
Switching Frequency (f_s)	DCM	100 kHz
	BCM	100 ~ 300 kHz

TABLE II
MAJOR COMPONENT LIST

Main Switch (S_1, S_2)		BSC190N15NS3 × 2
Output Diode (D_1, D_2)		IDB06S60C
Auxiliary Switch (S_{a1}, S_{a2})		IPD320N20N3G
Unfolding Bridge Switch (S_3 – S_6)		TK39J60W5
Transformer (TR_1, TR_2)	Core Type	RM14 – N97
	Turns Ratio (N)	6
	Magnetizing Inductance (L_{m1}, L_{m2})	6.15μH, 6.18μH
	Leakage Inductance (L_{lk1}, L_{lk2})	0.033μH, .037μH
Snubber Capacitor (C_s)		1.68 nF
Output Filter	Inductor (L_f)	220 μH
	Capacitor (C_f)	220 nF

IV. EXPERIMENTAL RESULTS

To verify the effectiveness of the proposed adaptive snubber, a 250 W flyback micro-inverter prototype has been built as shown in Fig. 10.

Tables I and II show the system specifications and the major component list used in the hardware, respectively. Based on (12) and the measured values of $C_{\rm pw} = 1.88$ nF, $C_D = 35$ pF, $C_{oss-20\rm V} = 3.8$ nF (accumulative C_{oss} of two parallel MOSFETs at 20 V), and the maximum overshoot of 130 V on the MOSFETs, the final snubber capacitance was selected as 1.68 nF.

The overall control schemes is implemented on a dsPIC microcontroller *dsPIC33FJ16GS504* as shown in Fig. 11. During the DCM and BCM operations, the turn-off timings of the main switches are determined by comparing the reference current with the instantaneous current of the primary side of each transformer. The constant frequency operation determines the turn-on timings of the switches in the DCM. However, in BCM, the turn-on timing of the main switch S_1 is determined by detecting zero voltage across v_{ds1}, instead of sensing the output diode current, and the turn-on timing of the main switch S_2 is synchronized to the turn-off timing of S_1 for simple interleaved operation.

The experimental results of the micro-inverter with the proposed adaptive snubber and without considering the MPPT [21], [22] operation are presented in Figs. 12–15 for the output power of 210 W, which corresponds to the maximum efficiency of the converter.

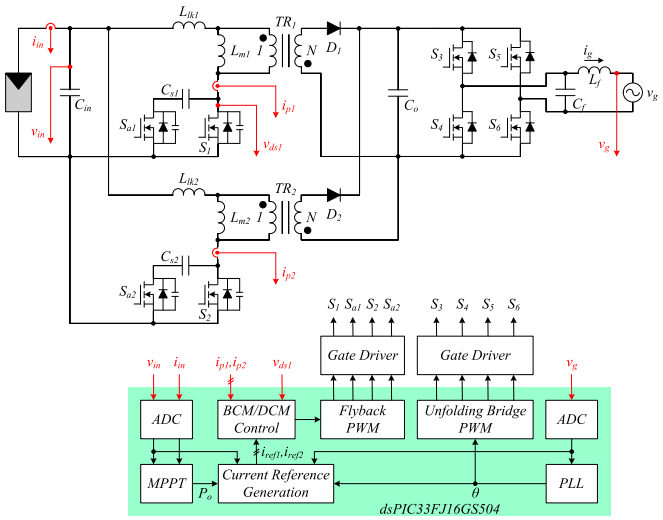

Fig. 11. Control block diagram of the flyback micro-inverter.

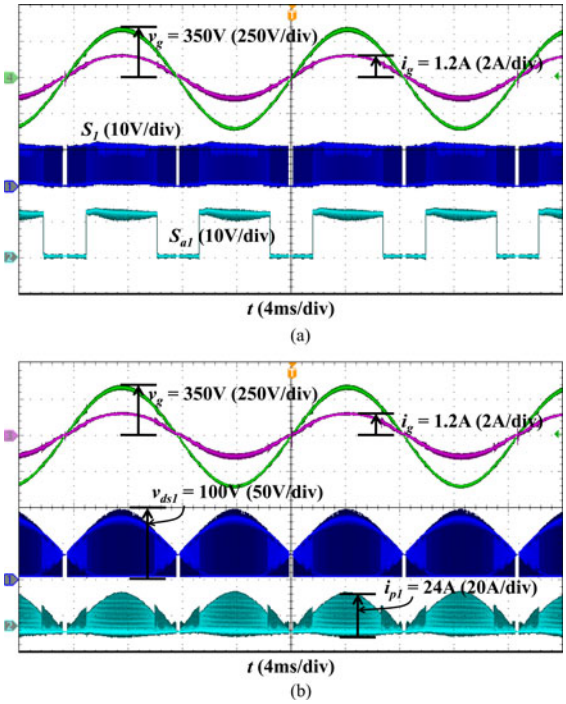

Fig. 12. Experimental waveforms. (a) Grid voltage v_g, grid current i_g, gate-to-source voltage of the main switch S_1, and gate-to-source voltage of the auxiliary switch S_{a1}. (b) Grid voltage v_g, grid current i_g, drain-to-source voltage of S_1 v_{ds1}, and primary side current of the transformer i_{p1}.

Fig. 12 shows the overall operational waveforms across the grid cycle. The grid current is synchronized with the grid voltage by phase-locked loop (PLL). The auxiliary switch S_{a1} gating signal in Fig 12(a) illustrates the 120-Hz operation of this switch and also the DCM-BCM mode transition during the operation of the converter.

Fig. 13 illustrates the interleaved operation of the converter in the BCM. It is shown in this figure that the turn-on timing of the main switch S_2 is synchronized with the turn-off timing of the main switch S_1.

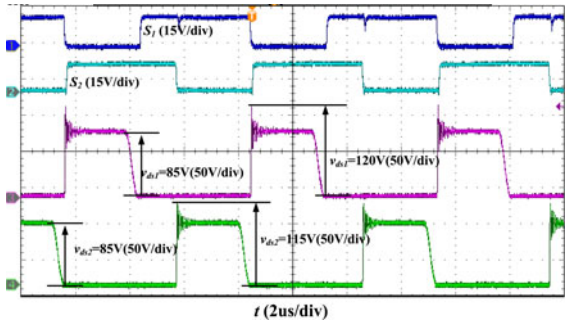

Fig. 13. Interleaved operation waveforms: Gate-to-source voltage of the main switch (S_1, S_2), drain-to-source voltage of the main switch (v_{ds1}, v_{ds2}).

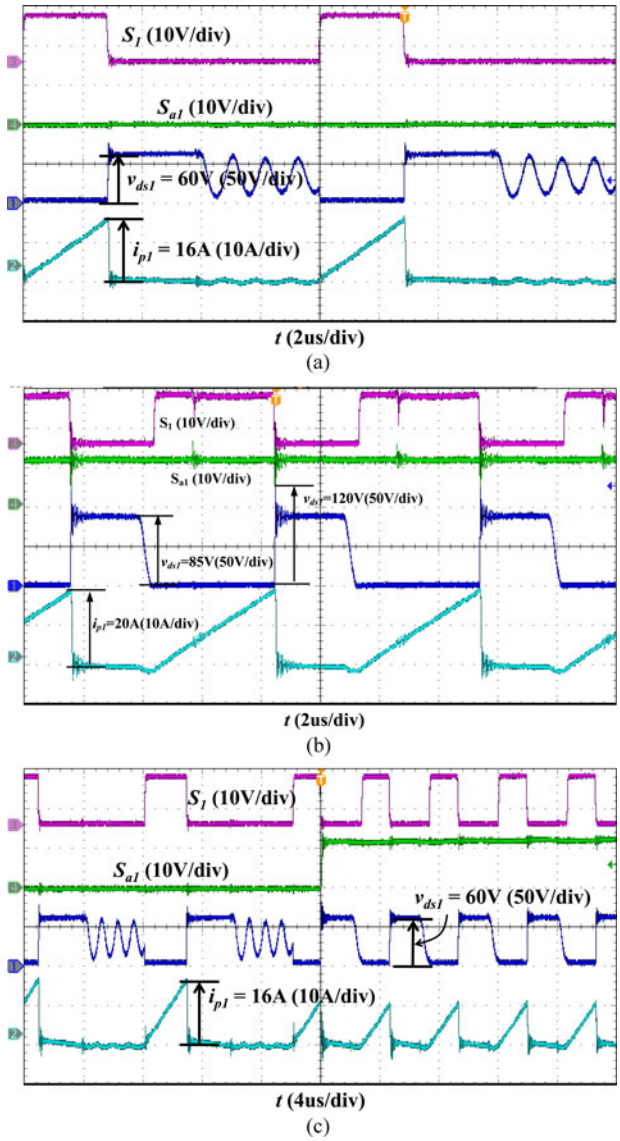

Fig. 14. Gate-to-source voltage of the main switch S_1, Gate-to-source voltage of the auxiliary switch S_{a1}, drain-to-source voltage of S_1 v_{ds1}, and primary side current of the transformer i_{p1}. (a) DCM operation. (b) BCM operation. (c) Mode transition between DCM and BCM.

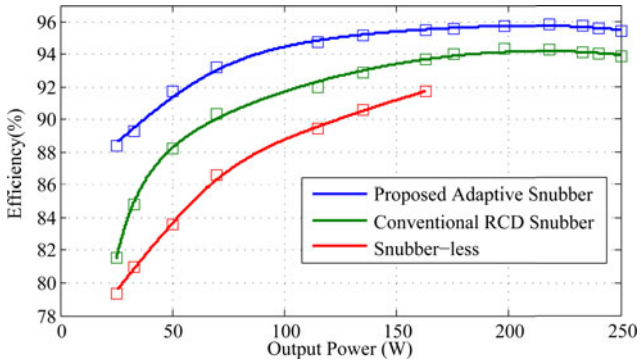

Fig. 15. Efficiency curve.

Fig. 14 shows the detailed waveforms in each operation mode. Fig. 14(a) and (b) shows the DCM and the BCM operations, respectively. In DCM, the auxiliary switch S_{a1} is turned OFF, and switch S_1 is hard switched. However, in BCM, the auxiliary switch S_{a1} is turned ON so that the snubber capacitor helps to decrease the overshoot of the voltage v_{ds1} as well as the turn-off switching loss by slow rising slope of the voltage v_{ds1}. Also, the capacitance energy is fully transferred to the input source by resonance with the magnetizing inductance before the next turn-on of the main switch S_1, so it does not cause any additional loss. Fig. 14(c) shows the mode transition waveform from DCM to BCM.

The efficiency of the prototype from the input port to the output port (including the micro-processor and driving power) was measured as shown in Fig. 15. The maximum efficiency is 95.8% and the CEC weighted efficiency is 94.6%.

The efficiency of the converter is also measured using a conventional RCD snubber ($C_{\rm snub} = 1.68\,{\rm nF}$ and $R_{\rm snub} = 4.3\,{\rm k}\Omega$) and it is shown in Fig. 15. The maximum achieved efficiency in this case is 94.4% with the CEC efficiency of 92.6%.

The operation of the flyback micro-inverter without any type of snubber or clamp circuit is evaluated and the resulted efficiency is demonstrated in Fig. 15. It should be mentioned that without snubber, the operation of the inverter was only possible up to 65% of the nominal power (160 W) as the maximum voltage overshoot reached the breakdown voltage of the MOSFETs.

V. Conclusion

This study presented a new adaptive snubber for the hybrid (DCM–BCM) operation of the flyback micro-inverter. The proposed adaptive snubber consists of the minimum number of components, namely, a small auxiliary switch and a small capacitor. It also exploits the parasitic capacitors of the flyback circuit (the main switch C_{oss}, transformer winding capacitor, and secondary rectifier capacitor) to further reduce the required value of the snubber capacitor. Furthermore, the auxiliary MOSFET switches at only double-line frequency and shares the same source terminal with the main switch of the flyback, which reduces the cost and complexity controller and the gate drive circuit.

Based on the detailed operation principal of the snubber circuit and the presented mathematical formulas, the criterial for selecting the proper snubber capacitor along with the consideration for the optimum design aiming to higher efficiency was presented.

The experimental results on a 250 W hardware prototype demonstrate that the proposed adaptive snubber is able to limit the voltage overshoot across the main switch and achieves high system efficiency through enabling the use of lower voltage MOSFET and also providing soft switching. The overall system with the proposed snubber achieved the maximum efficiency of 95.8% and the CEC weighted efficiency of 94.6%.

References

[1] Q. Li and P. Wolfs, "A review of the single phase photovoltaic module integrated converter topologies with three different DC link configurations," *IEEE Trans. Power Electron.*, vol. 23, no. 3, pp. 1320–1333, May 2008.
[2] H. Hu, S. Harb, N. Kutkut, I. Batarseh, and Z. J. Shen, "A review of power decoupling techniques for micro-inverters with three different decoupling capacitor locations in PV systems," *IEEE Trans. Power Electron.*, vol. 28, no. 6, pp. 2711–2726, Jun. 2013.
[3] D. Meneses, F. Blaabjerg, Ó. García, and J. A. Cobos, "Review and comparison of step-up transformerless topologies for photovoltaic AC-module application," *IEEE Trans. Power Electron.*, vol. 28, no. 6, pp. 2649–2663, Jun. 2013.
[4] M. Gao, M. Chen, C. Zhang, and Z. Qian, "Analysis and implementation of an improved flyback inverter for photovoltaic AC module applications," *IEEE Trans. Power Electron*, vol. 29, no. 7, pp. 3428–3444, Jul. 2014.
[5] A. C. Kyritsis, E. C. Tatakis, and N. P. Papanikolaou, "Optimum design of the current-source flyback inverter for decentralized grid-connected photovoltaic systems," *IEEE Trans. Energy Convers.*, vol. 23, no. 1, pp. 281–293, Mar. 2008.
[6] Y.-H. Kim, J.-W Jang, S.-C Shin, and C.-Y Won, "Weighted-efficiency enhancement control for a photovoltaic AC module interleaved flyback inverter using a synchronous rectifier," *IEEE Trans. Power Electron.*, vol. 29, no. 12, pp. 6481–6493, Dec. 2014.
[7] J. Zhang, X. Huang, X. Wu, and Z. Qian, "A high efficiency flyback converter with new active clamp technique," *IEEE Trans. Power Electron.*, vol. 25, no. 7, pp. 1775–1785, Jul. 2010.
[8] A. C. Nanakos, E. C. Tatakis, and N. P. Papanikolaou, "A weighted-efficiency-oriented design methodology of flyback inverter for AC photovoltaic modules," *IEEE Trans. Power Electron.*, vol. 27, no. 7, pp. 3221–3233, Jul. 2012.
[9] Y.-H. Kim, Y.-H. Ji, J.-G. Kim, Y.-C. Jung, and C.-Y. Won, "A new control strategy for improving weighted efficiency in photovoltaic AC module-type interleaved flyback inverters," *IEEE Trans. Power Electron.*, vol. 28, no. 6, pp. 2688–2699, Jun. 2013.
[10] Z. Zhang, X.-F. He, and Y.-F. Liu, "An optimal control method for photovoltaic grid-tied-interleaved flyback micro-inverters to achieve high efficiency in wide load range," *IEEE Trans. Power Electron.*, vol. 28, no. 11, pp. 5074–5087, Nov. 2013.
[11] N. Sukesh, M. Pahlevaninezhad, and P. K. Jain, "Analysis and implementation of a single-stage flyback PV microinverter with soft switching," *IEEE Trans. Ind. Electron*, vol. 61, no. 4, pp. 1819–1833, Apr. 2014.
[12] Y. Li and R. Oruganti, "A low cost flyback CCM inverter for AC module application," *IEEE Trans. Power Electron.*, vol. 27, no. 3, pp. 1295–1303, Mar. 2012.
[13] F. F. Edwin, W. Xiao, and V. Khadkikar, "Dynamic modeling and control of interleaved flyback module-integrated converter for PV power applications," *IEEE Trans. Ind. Electron.*, vol. 61, no. 3, pp. 1377–1388, Mar. 2014.
[14] T. V. Thang, N. M. Thao, J.-H Jang, and J.-H Park, "Analysis and design of grid-connected photovoltaic systems with multiple-integrated converters and a pseudo-DC-link inverter," *IEEE Trans. Ind. Electron.*, vol. 61, no. 7, pp. 3377–3386, Jul. 2014.
[15] S. Zengin, F. Deveci, and M. Boztepe, "Decoupling capacitor selection in DCM flyback PV microinverters considering harmonic distortion," *IEEE Trans. Power Electron.*, vol. 28, no. 2, pp. 816–825, Feb. 2013.
[16] H. Hu, S. Harb, X. Fang, D. Zhang, Q. Zhang, Z. J. Shen, and I. Batarseh, "A three-port flyback for PV micro-inverter applications with power pulsation decoupling capability," *IEEE Trans. Power Electron.*, vol. 27, no. 9, pp. 3953–3964, Sep. 2012.

[17] H. Hu, S. Harb, N. H. Kutkut, Z. J. Shen, and I. Batarseh, "A single-stage micro-inverter without using electrolytic capacitors," *IEEE Trans. Power Electron.*, vol. 28, no. 6, pp. 2677–2687, Jun. 2013.
[18] Z. Zhang, M. Chen, W. Chen, C. Jiang, and Z. Qian, "Analysis and implementation of phase synchronization control strategies for BCM interleaved flyback microinverters," *IEEE Trans. Power Electron.*, vol. 29, no. 11, pp. 5921–5932, Nov. 2014.
[19] Q. Mo, M. Chen, Z. Zhang, Y. Zhang, and Z. Qian, "Digitally controlled active clamp interleaved flyback converters for improving efficiency in photovoltaic grid-connected micro-inverter," in *Proc. IEEE 27th Annu. Power Electron. Conf. Expo.*, Feb. 2012, pp. 555–562.
[20] H. K. Patel, "Voltage transient spikes suppression in flyback converter using dissipative voltage snubbers," in *Proc. IEEE 3rd Conf. Ind. Electron. Appl.*, Jun. 3–5, 2008, pp. 897–901.
[21] G. Farivar, B. Ashaei, and S. Mehrnami, "An analytical solution for tracking photovoltaic module MPP," *IEEE J. Photovolt.*, vol. 3, no. 3, pp. 1053–1061, Jul. 2013.
[22] G. Farivar, B. Asaei, and M. A. Rezaei, "A novel analytical solution for the PV-arrays maximum power point tracking problem" in *Proc. IEEE Int. Conf. Power Energy*, Nov. 29, 2010–Dec. 1, 2010, pp. 917–922.

Mohammad Ali Rezaei received the B.Sc. and M.Sc. degrees in electrical engineering from the University of Tehran, Tehran, Iran, in 2008 and 2011, respectively. He is currently working toward the Ph.D. degree in the Future Renewable Electric Energy Delivery and Management Systems Center of North Carolina State University, Raleigh, NC, USA.

His research interests include high-power electronics and renewable energy grid integration systems.

Kui-Jun Lee received the B.S. and Ph.D. degrees in electrical engineering from Hanyang University, Seoul, Korea, in 2005 and 2012, respectively.

From 2012 to 2014, he was a Postdoctoral Researcher at FREEDM Systems Center, North Carolina State University, Raleigh. Since 2014, he has been with Samsung Electronics, Suwon, Korea, where he is currently a Senior Engineer. His research interests include power converter system for renewable energies and soft-switching techniques.

Alex Q. Huang (S'91–M'94–SM'96–F'05) was born in Zunyi, Guizhou, China. He received the B.Sc. degree from Zheijiang University, Zheijiang, China, in 1983, and the M.Sc. degree from the Chengdu Institute of Radio Engineering, Chengdu, China, in 1986, both in electrical engineering. He received the Ph.D. degree from Cambridge University, Cambridge, U.K., in 1992.

From 1992 to 1994, he was a Research Fellow at Magdalene College, Cambridge. From 1994 to 2004, he was a Professor at the Bradley Department of Electrical and Computer Engineering, Virginia Polytechnic Institute and State University, Blacksburg, VA, USA. Since 2004, he has been with North Carolina State University, Raleigh, NC, USA, and is currently the Progress Energy Distinguished Professor of electrical and computer engineering. He established the NSF FREEDM Systems ERC and served as the Director from 2008 to 2014. Since 1983, he has been involved in the development of modern power semiconductor devices and power integrated circuits. He fabricated the first IGBT power device in China in 1985. He is the inventor and key developer of the emitter turn-off thyristor technology. He developed the concept of Energy Internet and the key smart transformer-based energy router technology. His current research interests include power electronics, power management microsystems, and power semiconductor devices. He has published more than 400 papers in international conferences and journals, and has been granted more than twenty U.S. patents.

Dr. Huang has mentored and graduated more than 70 Ph.D. and master students. He received the NSF CAREER Award, the prestigious R&D 100 Award, and the MIT Technology Review's 2011 Technology of the Year award.